Cerium modified birnessite-like MnO2 for low temperature oxidation of formaldehyde: Effect of calcination temperature

Grece Abdallah, Jean-Marc Giraudon, Nicolas Nuns, Ahmed Addad, R. Morent, N. de Geyter, Jean-Francois Lamonier

Cerium modified birnessite-like MnO_2 for low temperature oxidation of formaldehyde: Effect of calcination temperature.

Grêce Abdallah[a,c], Jean-Marc Giraudon[a*], Nicolas Nuns[b], Ahmed Addad[c], Rino Morent[d], Nathalie De Geyter[d], Jean-François Lamonier[a].

[a]*Univ. Lille, CNRS, Centrale Lille, Univ. Artois, UMR 8181 - UCCS - Unité de Catalyse et Chimie du Solide, Lille, 59000, France*

[b]*Univ. Lille, CNRS, Centrale Lille, Univ. Artois, IMEC-Institut Michel-Eugène Chevreul, Lille, 59000, France*

[c]*Unité Matériaux et Transformations (UMET), UMR 8207, Université de Lille, CNRS, INRAE, Centrale Lille, Lille, F-59000, France*

[d]*Ghent University, Faculty of Engineering and Architecture, Department of Applied Physics, Research Unit Plasma Technology, Sint-Pietersnieuwstraat 41 B4, 9000 Ghent, Belgium*

**Corresponding author: jean-marc.giraudon@univ-lille.fr*

Abstract

Cerium modified birnessite-like MnO_2 were synthesized (Ce_xMn; x = 0.01; 0.1) from a simple and inexpensive redox method involving the reduction of potassium permanganate by sodium lactate in the presence of $Ce(NO_3)_3$ at ambient temperature. The as-synthesized samples were calcined at different temperatures (Tc: 200, 300 and 400 °C) to be tested in HCHO total oxidation in dry air at low temperature. The $Ce_{0.01}Mn$ catalyst calcined at 400 °C showed the best catalytic activity in HCHO oxidation with a T_{50} (temperature at which 50 % of HCHO was converted into CO_2) of 50 °C and was found to be air and moisture stable (up to 75 %RH) upon time. The beneficial effects of a calcination step at 400 °C allowed to get enhanced asymmetric Ce-O-Mn surface interactions along with highly dispersed $Ce^{4+/3+}$ related species and enhanced $^{TC}Mn^{3+}$ (TC: triple corner) amounts which contributed to a great extent for its high activity in HCHO oxidation.

Keywords: Cerium modified birnessite, HCHO oxidation, calcination, ToF-SIMS

1. Introduction

Among the various volatile organic compounds (VOCs), formaldehyde (HCHO) is considered as one of the most hazardous pollutants, especially in an indoor environment. Formaldehyde which is mainly emitted from construction and decoration materials can lead to an increased risk of developping physical and mental illness at elevated concentrations. Besides, it has been shown that a chronical exposure to a formaldehyde environment can result in naso pharyngeal cancer and other serious diseases [1,2].

Different approaches for HCHO removal from air have been proposed such as adsorption [3,4], plasma technology [5], photocatalysis [6,7] and catalytic oxidation [8,9]. Among these different approaches, low temperature - preferably room temperature - heterogeneous catalytic oxidation has been recognized to be one of the most efficient technologies for HCHO removal [10–12]. The success of such a technology depends greatly on the catalytic properties in total HCHO oxidation. The desired cost-effective catalyst should be able to work efficiently at low temperature in a moist atmosphere.

Supported noble metal catalysts exhibit high activity allowing total HCHO oxidation into CO_2 and H_2O at room temperature [13,14]. However, their high costs and lack of resources impede their practical applications [10,15,16]. Therefore, the development of less expensive active phases is highly desirable for a large-scale application [12,17,18]. In 2002, Sekine *et al.* [19] found MnO_2 as the most active noble metal-free catalyst in HCHO oxidation among various commercial transition metal oxides (TMO). Furthermore, MnO_2 has advantages to be cost-effective, environmentally friendly and easy to get. Since then, different investigations were carried out to improve the catalytic activity of MnO_2 for HCHO oxidation [20–28]. In terms of MnO_2 crystal structure, birnessite-type MnO_2 was recognized to be the most active catalyst in HCHO oxidation [15]. Birnessite-type MnO_2 is a two-dimensional layered structure,

composed of alternating stacked Mn–O layers (edge-shared MnO_6 octahedra) and hydrated alkali cations (Na^+, K^+, etc.) restricted in the interlayer region [29–32]. In order to promote the catalytic performances of such layered materials in HCHO oxidation significant experimental researches have recently been carried out.

Wang *et al.* [33] reported on the positive effect of manganese vacancies on the activity. The content of manganese vacancies (V_{Mn}) in K-birnessite synthesized from a redox-precipitation route was tuned by affecting the initial oxidant/reductant atomic ratio. MnO_2 with the highest content of V_{Mn} showed the best activity for formaldehyde decomposition. The presence of K^+ located nearby V_M sites in HCHO oxidation has been shown to facilitate the formation of surface active oxygen species. In addition, Rong *et al.* [34] reported about the existence of an optimal K^+ content to promote the activity in Mn vacancy-rich birnessite-type. A too high K^+ content increased the amount and strength of surface basic sites making the CO_2 desorption more difficult and, in that way, partially inhibited the catalyst. Taking these considerations into account, Ji *et al.* [35] reported on K-birnessite with poor cystallinity with a medium K^+ concentration to obtain a highly active birnessite in HCHO oxidation.

Element incorporation was also another followed strategy to obtain a more active catalyst. In that way, incorporation of suitable transition metals (TM) or rare earth elements (RRE) was investigated to promote activity by seeking to decrease energy formation of oxygen vacancy [36]. A synergistic effect was observed over MnO_2(x)-CeO_2 catalysts on activity due to MnO_2/CeO_2 interactions which induced a mean crystallite size decrease, high Mn^{3+}/Mn and O_{ads}/O_{latt} surface atomic ratios [37]. Liu *et al.* [38] investigated the performances of MnO_x-CeO_2 catalysts with different Mn/Ce ratios in HCHO oxidation. The enhancement of reactivity in HCHO oxidation was ascribed to the activation of lattice oxygen species in MnO_x due to CeO_2 addition. Following a strategy of rational design of defects to enhance catalytic activity, Zhu *et al.* [39] reported on the performances for HCHO oxidation of Ce modified-type MnO_2

with different Ce/Mn ratios obtained from a redox-precipitation method carried out at 90 °C followed by a drying step at 105 °C for 12 h. Ce-MnO_2 (1:10) has proved to be the most effective catalyst. The creation of grain boundaries, oxygen vacancies and enrichment of surface-active oxygen species were postulated to be responsible for its high activity in HCHO oxidation.

Recently, Wang *et al.* [40] have reported on the beneficial role of interspacing water to promote the formaldehyde decomposition. Adsorbed formaldehyde, which is promoted by bonded water via hydrogen bonding, is transformed into formate and carbonate with the consumption of hydroxyl and bonded water. Both bonded water and water in air can compensate the consumed hydroxyl groups to sustain the mineralization of formaldehyde at room temperature. The authors have also highlighted the beneficial role of K^+ as interspacing cation [18] which is believed to enhance the surface oxygen activity facilitating the regeneration of surface hydroxyls by activating H_2O. C. Mang *et al.* [41] investigated the catalytic oxidation of HCHO in moist air on birnessites whose water content was adjusted through calcination up to 500 °C. It was shown that the non-calcined birnessite exhibited the superior catalytic activity. Absorbed and molecular water components could react with active oxygen species (O_2^-, O^- …) around the oxygen vacancy to replenish the consumed surface hydroxyl groups which were involved in the destruction of HCHO and intermediates. Water content in air stream sustained water supply to the birnessite.

The objective of the present work is to investigate the effect of the temperature of calcination over Ce modified birnessite-MnO_2 (Ce/Mn = 0.01; 0.1) synthesized by a redox-precipitation method on the physico-chemical properties and catalytic performances for complete oxidation of HCHO oxidation in dry and humid air.

2. Experimental

2.1.Synthesis of birnessite and Ce-doped birnessites

Birnessite was prepared following a redox method inspired from that of Händel *et al.* [42]. Typically, 4.0 g (25.3 mmol) of $KMnO_4$ (Fluka, ≥ 99 %) was dissolved into 400 mL of distilled water under stirring (350 rpm). 4 mL (22.54 mmol) of $NaC_3H_5O_3$ (50 % w/w) (Fisher Chemical, solution 60% w/w) was added dropwise to the aqueous $KMnO_4$ solution. The resulting brown suspension was stirred for 2 h. After centrifugation (4000 rpm for 20 min) the collected brown precipitate was washed 2 times (25 mL of distilled water each time) and finally dried in an oven at 40 °C for 48 h to give a black powder Mn-B. The Ce-modified MnO_2 (Ce_xMn; x: Ce/Mn atomic ratio of 0.01; 0.1) were prepared based on the same procedure except that Ce $(NO_3)_3.6H_2O$ (Alfa Aesar; ≥ 99.5 %) was dissolved concomitantly with $KMnO_4$. The samples Ce_xMn; x: 0.01; 0.1) were calcined at 200 °C (only for x = 0.1), 300 °C and 400 °C. The calcined samples were labelled Ce_xMn-X00, with X00 standing for the calcination temperature.

2.2. Characterization

The elemental analysis was performed by Inductively Coupled Plasma-Optic Emission Spectroscopy 720-ES ICP-OES. X-ray diffraction patterns (XRD) were collected on a D8 Advanced Bruker AXS diffractometer equiped with Cu $K_{\alpha 1}$ monochromatic radiation source (λ = 1.5406 Å) and LYNXEYE super speed detector with the power set at 40 kV and 40 mA. The X-ray diffraction patterns were recorded within the 5 °-80 °C with a 0.02 ° step size in 2θ (step time = 1 s). An amorphous SiO_2 holder and modified XRD conditions of 10-20 ° in the 2 theta range with step size of 0.2 ° and step time of 5 s were used to estimate the interspacing distance d(100). Thermal analyses (TGA/DSC) were carried out on 10 mg of sample in dry flowing air (100 mL/min) with a heating rate of 10 °C/min up to 800 °C using a DSC-TGA

SDT 2960 of TA Instruments. N_2 physisorption isotherms were recorded at -196 °C using a gas sorption analyzer TriStar II 3020 from Micromeretics. Prior to analysis, the samples were heated at 100 °C for 4 h under dynamic vacuum (0.05 mbar). The Brunauer-Emmett-Tellller (BET) method was used to calculate the specific surface areas.

Transmission electron microscopy (TEM) characterization was performed using a TECNAI TEM operated at 200 kV. The prepared powders were deposited onto a carbon-coated copper grid for TEM observation. High-angle annular dark field imaging during TEM was performed on a FEI Titan themis 300, equipped with a C_s probe corrector and a High-efficiency Super-X detector (EDX). At 300 kV in HRSTEM mode it was possible to reach a resolution of 0.7 Å. X-ray photoelectron spectroscopy (XPS) experiments were performed using an AXIS Ultra DLD Kratos spectrometer equipped with a monochromatic aluminum source (Al K_α = 1486.7 eV) and charge compensation gun. The binding energies (BE) were referenced from adventitious C 1s at 284.8 eV. High resolution spectra were collected with a constant pass energy (40 eV). Quantification and spectral decomposition were processed using CasaXPS® software. Quantification was performed based on Mn 2p, Ce 4d, K 2p, O 1s, Na 1s and C 1s. The Mn $2p_{3/2}$ envelope was decomposed considering a Mn^{4+} (MnO_2)/Mn^{3+} (Mn_2O_3) mixture in accordance with the procedure of M. Biesinger [43]. The Ce 4d core-level was considered for quantification instead of Ce 3d due to Ce 3d/Auger Mn LMM peak overlap.

Attenuated Total Reflectance - Fourier Transform Infrared Spectroscopy (FTIR-ATR) spectra were collected on a Thermo Scientific iS50 FTIR spectrometer. 256 scans were collected with an instrument resolution of 2 cm^{-1} over the spectral range extending from 4000 to 200 cm^{-1}. H_2-Temperature Programmed Reduction (H_2-TPR) was performed on a Micromeritics Autochem II 2920 instrument. 50 mg of sample was placed in a U-shaped tubular quartz reactor. The samples were pre-treated in flowing Ar at 150 °C for 1 h followed by cooling

down the temperature. The cleaned catalysts were exposed to a 5 vol.% H_2/Ar gas mixture with a flow rate of 50 mL/min from 25 °C to 800 °C at a heating rate of 10 °C/min.

ToF-SIMS data were acquired using a ToF-SIMS5 spectrometer (ION-TOF GmbH Germany) equipped with a bismuth liquid metal ion gun (LMIG). The powders were crushed using an agate mortar and pestle and the standard tablets were prepared using a press machine. The samples were bombarded with a pulsed Bi_3^+ primary ion beam (25 keV, 0.25 pA) rastered over a 100 µm x 100 µm surface area (128 x 128 pixels and 100 scans). The total fluence did not amount up to 10^{12} ions/cm^2 ensuring static conditions. Charge effects were compensated by means of a 20 eV pulsed electron flood gun. With a cycle time of 200 µs, data were collected over a mass range m/z = 0-3500 for both positive and negative secondary ions. The fragments were identified by their exact mass, coupled with the appropriate intensities for the expected isotope pattern. The mass resolution m/Δm at m/z = 55 for Mn^+ was 2500.

2.3. Catalytic oxidation of formaldehyde

2.3.1. Light-off curves

Oxidation of formaldehyde was carried out a fixed bed reactor (inner diameter of 8 mm) loaded with 100 mg of catalyst (100-200 µm). Gaseous formaldehyde was produced from para-formaldehyde in a permeation tube incorporated in a permeation chamber from VICI (Dynacalibrator, VICI Metronics, Inc.). Catalyst activation was carried out over the calcined Ce_xMn pretreated *in situ* at 200 °C for 1 h in 20 vol% O_2/N_2 (100 mL/min). Afterwards, the stabilized reactive flow consisting of 100 ppmv of HCHO mixed with 20 vol% O_2/N_2 was sent towards the fixed bed reactor for 1 h. At that time the temperature was allowed to decrease from 200 °C to 25 °C at a rate of 0.2 °C/min. The total flow rate of 100 mL/h allowed to get a gas hourly space velocity (GHSV) of 60 L/(g_{cat}.h). The gaseous species exiting the reactor were analyzed on line by a micro GC (CP4900; VARIAN), equipped with a thermal conductivity

detector. Separations were carried out using two columns: one CP-Sil5 CB column channel (8 m) for HCHO analysis and one COX column channel for CO_2 analysis. The HCHO elimination corresponding to the HCHO removal efficiency from the gas phase was expressed by the HCHO conversion (eq.1) while the HCHO oxidation in CO_2 was expressed from the CO_2 yield (eq.2) as follows:

$$\text{HCHO elimination (\%)} = \frac{[\text{HCHO}]_{\text{in}} - [\text{HCHO}]_{\text{out}}}{[\text{HCHO}]_{\text{in}}} \times 100 \quad (1)$$

$$\text{HCHO conversion (\%)} = \frac{[\text{CO}_2]_{\text{out}}}{[\text{HCHO}]_{\text{in}}} \times 100 \quad (2)$$

$[HCHO]_{out}$ and $[CO_2]_{out}$ were the outlet HCHO and CO_2 concentrations and $[HCHO]_{in}$ the initial HCHO concentration (100 ppmv).

2.3.2. Effect of stability and moisture

Catalyst activation was carried out over the calcined Ce_xMn-400 adopting a similar procedure as given above. The reactor was then cooled down to 50 °C in flowing dry air. Afterwards, the stabilized reactive flow (100 ppmv of HCHO diluted in 20 vol% O_2/N_2) was sent towards the fixed bed reactor and RH was allowed to increase with time. The duration and RH% of the successive steps were specified in the appropriate figures in the text. At the end of the test the reactor was cooled down in static air. The suffix SF was added for the labelling of the used catalysts.

3. Results and discussion

3.1. Characterization of samples

Results of ICP-OES analyses are reported in **Table 1.** For Mn-B, the K/Mn and Na/Mn atomic ratios of 0.39 and 0.059 are substantially higher than those of 0.13 and 0.04 obtained by Händel *et al.* [42]. Differences in initial reactant ratios and experimental procedures may account for such discrepancies. Thus, these overall results leave open the possibility of the existence of mixed (Na,K)-birnessites which is supported by previous thermodynamic studies [44]. In that sense, intercalated cation exchange in birnessite monitored by real-time XRD analysis has been shown to involve continuous shifts in atomic positions rather than the co-existence of end-member configurations [45] which is in contrast to the results of Putnis *et al.* [46] who postulate that exchange processes occur through dissolution of one phase and precipitation of another. For the Ce modified MnO_2 samples, the atomic Ce/Mn ratios are consistent with the nominal ones and the K/Mn and Na/Mn atomic ratios are rather similar to those found for the Ce-free sample.

TG analyses have been performed on the as-synthesized samples in order to monitor the weight loss evolution with increasing temperature (**Fig. 1(a,b)** and **Table 2**). The TG curve of Mn-B shows two distinct weight losses. The first weight loss of 10.7 %, below 220 °C, has been ascribed to the successive release of adsorbed and interlayer water [47], respectively, while the second one of 5.1 wt% has been attributed both to dehydroxylation of layer OH groups [40] and oxygen release from MnO_2 layers [47, 48] leading to the partial reduction of Mn^{4+} into Mn^{3+} by use of the following equation :

$$–Mn^{4+}–O^{2-}–Mn^{4+} \rightarrow \quad Mn^{3+} \square\ Mn^{3+} + ½\ O_2 \qquad (1)$$

Migration of Mn^{3+} cations from layer to interlayer to release strain takes place afterwards and before birnessite (δ-MnO_2) to cryptomelane (α-MnO_2) solid-state transformation [49]. This diffusional process has been recognized to affect the density of layer and interlayer Mn^{3+} in the

phyllomanganate structure. The TG curves of the fresh Ce modified like-birnessites look rather similar to that of the Ce-free sample. Due to modification with cerium, new linkage possibilities may arise from octahedral layer framework oxygen release:

$$–Ce^{4+}–O^{2-}–Mn^{3+} \rightarrow Ce^{3+} \square Mn^{2+} + ½\ O_2 \quad (2)$$

$$–Ce^{4+}–O^{2-}–Ce^{4+} \rightarrow Ce^{3+} \square Ce^{3+} + ½\ O_2 \quad (3)$$

$$–Ce^{4+}–O^{2-}–Mn^{4+} \rightarrow Ce^{3+} \square Mn^{3+} + ½\ O_2 \quad (4)$$

It is worthy to note that a distinct weight gain is observed which is ascribed to the incorporation of oxygen into the materials resulting from the oxidation of Mn^{3+} into Mn^{4+} as a result of δ-MnO_2 to α-MnO_2 transformation [32,50]. In any case, α-MnO_2 (**Fig. S1**) has been detected using XRD after TG experiments along with the detection of a K-rich birnessite (hexagonal unit cell, space group = P63/mmc, a = 2.84 Å, and c = 14.16 Å) [51, 52] as minor phase for $Ce_{0.01}Mn$ and the presence of the well cristallized cubic phase of CeO_2 for $Ce_{0.1}Mn$. It is worth mentioning that this oxygen uptake which is correlated to the degree of reduction of the Ce modified birnessite-like MnO_2 sample increases by a factor 4 with a 10-fold increase of the Ce/Mn atomic ratio. This solid-state transformation occurs at 520 °C for $Ce_{0.01}Mn$ and is shifted to 680 °C for $Ce_{0.1}Mn$ indicating thermal stability improvement with increasing Ce content. Hence, tuning the properties of the Ce modified birnessites through successive dehydration, dehydroxilation and oxygen release processes are expected to occur by increasing the temperature of calcination before solid state layer-tunnel transformation takes place.

The XRD patterns of the as-synthesized and calcined samples are displayed in **Fig. 2a** and **2b**, respectively. Four peaks are observed for Mn-B consistent with a turbostratic birnessite δ-MnO_2 [53]. These peaks can be indexed to (001), (002), (11, 20) and (31, 02) respectively, based on a C-centered two-dimensional unit cell. Additionally,-the peaks observed at about 37.0 ° (2.42 Å) and 66.2 ° (1.41 Å) exhibit a d-spacing ratio of 1.72 close to $3^{1/2}$ which indicates a

pseudo-hexagonal symmetry in the manganese octahedral layer [54,55]. The symmetry of the peak profile at 66.2 ° also supports a layer unit-cell that is hexagonal [56]. For Ce/Mn = 0.01, the XRD pattern remains unchanged while for Ce/Mn = 0.1, the two peaks located at ~ 7.2 Å (001) and 3.5 Å (002) have practically disappeared. It is worthy to note that the mean crystallite size determined from XRD using the peak at ~ 66.2 ° decreases from 4.8 nm to ~ 3.2 nm when adding Ce (Table 3). After calcination, the (001) diffraction peak shifts to higher angle (**Fig. 2c**) indicating a shrinkage of the interlayer distance for Mn-B and $Ce_{0.01}Mn$ samples (7.20 Å (Mn-B) -> 6.87 Å (Mn-B-400); 7.32 Å ($Ce_{0.01}Mn$) -> 6.96 Å ($Ce_{0.01}Mn$-300) -> 6.75 Å ($Ce_{0.01}Mn$-400)). Additionally, it is clearly observed a hump at around 40-45° in 2θ (**Fig. S2**) for $Ce_{0.01}Mn$-400 previouly associated with triple-corner (TC) sharing configuration above or below the vacancy sites of Mn-layers [49]. Such observance suggests a higher density of Mn^{3+} at TC sites ($^{TC}Mn^{3+}$) when $Ce_{0.01}Mn$ has been calcined at 400 °C for 5 h. This finding agrees with a change of the spatial distribution of Mn^{3+} cations as enonced by S. Grangeon *et al.* [49] who have postulated migration of Mn^{3+} cations from layer to interlayer to release strains and their subsequent sorption above newly formed vacancy in TC sharing configuration prior vernadite to cryptomelane transformation. Besides, the presence of a low-intensity hump in the 2θ range of 25 ° to 35 ° for the calcined $Ce_{0.1}Mn$ samples has been assigned to the cubic phase of CeO_2 (JCPDS No.34-0394). All these findings agree with: (i) structural modifications when increasing Ce content, (ii) an interlayer spacing reduction as Tc increases and (iii) a non uniform Mn^{3+} distribution resulting to an increase of $^{TC}Mn^{3+}$ after calcination at 400 °C for $Ce_{0.01}Mn$.

Figs. S(3-5) present TEM images of the as-synthesized Mn-B, $Ce_{0.01}Mn$ and $Ce_{0.1}Mn$ samples at different magnifications. Agglomeration of particles is always seen at low magnifications. Based on HRTEM images, the average number of stacked layers (along c axis) is about 5-6 for Mn-B. Ce-coprecipitation does not cause so much change in layer stacking, likely due to the already low number of stacked layers for Mn-B. Conversely, the cluster density

of stacked layers is significantly decreased. The particle lateral length is in the range of 5-10 nm for Ce_xMn samples while this one of higher dimension for Mn-B cannot be obtained due to the superposition of the particles. The decrease of the lateral length of the particles is in line with Ce atoms located at the edges of the material which inhibit the growing of the particles. Regarding the $Ce_{0.1}Mn$ sample it is observed a blurred structure which can be linked to some extent to an increase of defects. For all samples, based on the Fast Fourier Transform (FFT) image given in inset the estimated interlayer spacing was 6.5 Å ± 0.2 Å slightly less to that reported previously of 0.71 nm for Ce-coprecipitated birnessite-like MnO_2 catalysts [39]. Elemental mapping of the as-prepared $Co_{0.1}Mn$ sample in **Fig. S6** shows that the Ce, K, Na elements are uniformly distributed. In order to study more precisely the dispersion of Ce in $Co_{0.1}Mn$ the high-angle annular dark-field imaging mode in high-resolution scanning transmission electron microscopy (HAADF-STEM) has been used. **Fig. 3(a-c)** presents representative HAADF-HRSTEM images of the as-synthesized $Ce_{0.1}Mn$ sample. Considering that the contrast in HAADF images depends strongly on Z number (O = 16, Na = 23, Mn = 25, K = 39, Ce = 140) and that the corresponding bright field images in **Fig. 3(d-e)** do not show a significant thickness it follows that the observed bright spots represent cerium species. For the as-synthesized Ce based solids it was not possible to observe CeO_2 particles. It is concluded that Ce interacts with birnessite through very small CeO_x clusters (and possibly individual atoms) decorating the birnessite layers.

In order to better apprehend the effect of calcination temperature on air exposed samples, TG analysis has been carried out on the *ex situ* calcined Ce-modified birnessite-type MnO_2 (**Fig. 1a** and **1b**) as δ-MnO_2 may be subject to partial rehydration when exposed to air [57]. It is noticed that the TG traces are quite similar to those of the as-synthesized catalysts but the weigh loss of each step decreases with increasing calcination temperature (**Table 2**). These observations show that the amount of adsorbed water has significantly decreased showing that

reintercalation of water into the interlayer spacing of the calcined Ce modified birnessite is reversible only to some extent and that its proportion decreases with increasing calcination temperature. A similar finding holds for hydroxylation/oxygen uptake from the layer framework. Hence water as well as structural hydroxyl and oxygen/manganese vacancy content can be regulated through calcination.

The nitrogen adsorption–desorption isotherms of the synthesized birnessite are shown in **Fig. S7**. Type-II isotherms with an H3 hysteresis loop are observed for as-synthesized and calcined Mn-B and $Ce_{0.01}Mn$ samples (**Fig. S7(a,b)**) while Type-IV isotherms are obtained with the based $Ce_{0.1}Mn$ samples with an H2 hysteresis loop which turns out to be a mixture of H3 and H4 after calcination at a temperature higher than 200 °C (**Fig. S7c**). Significant increase of specific area has been observed when adding cerium for the as-prepared samples (**Table 3**) due partly to a decrease of the mean crystallite size ascribed to the inhibitory effect of Ce on MnO_2 particle growth [39]. Hence, Ce acts as a structural promotor allowing the increase of catalyst specific surface. After calcination at 400 °C the specific area does not change significantly for $Ce_{0.01}Mn$ (~ 130 m^2/g) while a small decrease is observed for $Ce_{0.1}Mn$ whose specific area drops from 243 m^2/g to 196 m^2/g.

The surface chemical states and elemental compositions investigated by XPS are given in Table 3. The Mn 2p envelopes for cerium modified birnessite samples exhibite two peaks (not shown here) at 642 ± 0.2 eV and ~ 654 ± 0.2 eV which are ascribed to Mn $2p_{3/2}$ and Mn $2p_{1/2}$, respectively. Based on curve fitting of the Mn $2p_{3/2}$ core level XPS spectra displayed in **Fig. S8(a-c)** considering Mn^{4+} and Mn^{3+} contributions [43], it is shown that the Mn^{3+}/Mn^{4+} atomic ratio decreases for the Ce-coprecipitated samples. Conversely, the Mn^{3+}/Mn^{4+} ratio increases strongly after a calcination step at 400 °C to get a maxixum value of 0.37 for $Ce_{0.1}Mn$-400. As the presence of Mn^{3+} is related to the formation of surface oxygen vacancies to maintain electroneutrality, it is concluded that $Ce_{0.1}Mn$-400 ownes a large amount of oxygen vacancies.

Taking account of the Ce 4d XPS envelopes (**Fig. S8d**) it can be stated that Ce^{4+} appears as Ce predominant oxidation state for $Ce_{0.1}Mn$ [58]. Comparison of Ce/Mn atomic ratios estimated by XPS and ICP-OES analysis shows that Ce^{4+} are well dispersed in the MnO_2 matrix. It is also noticed that the calcination step also affects the alkali distribution as the K/Mn and especially the Na/Mn ratios decrease with increasing calcination temperature.

The redox properties of the as-synthesized and calcined samples have been assessed by H_2-TPR. As shown in **Fig. S9** four hydrogen consumption peaks marked as α, β, γ and δ are observed for all samples. Low temperature reduction peak (α) is due to the reduction of surface adsorbed oxygen species, the intermediate temperature reduction peak (β) is ascribed to surface lattice oxygen reduction and high temperature reduction peaks (γ, δ and λ) are related to bulk phase lattice oxygen reduction owing to $Na_xK_yMnO_2$ -> Mn_2O_3 (Mn_3O_4) -> MnO [39]. It is observed that the α-reduction peak areas of the Ce modified samples increase with increasing T_C. Additionally, it has been found an increase of the β-reduction peak areas (up to 300 °C) combined with a lowering of peak temperature with increasing T_C. Therefore, Ce addition promotes significantly the formation and mobility of surface active oxygen species [39,59] which is of prime importance for a better activity.

Static ToF-SIMS has been applied to the analysis of the samples as it supplies detailed information on the atomic and molecular composition of the uppermost layers [60]. ToF-SIMS spectra of the calcined Ce_xMn (x = 0.1; 0.01) have been compared with those of the as-synthesized compounds in order to investigate how the calcination affects the uppermost layers of the materials. It is observed for both cases an increase of the secondary ion intensity Ce^+/Mn^+ ratio after calcination (**Table 4**) which indicates a cerium enrichment due to the migration of Ce atoms to the surface. The Ce-containing secondary ions with one, two and three Ce atoms are respectively presented in three m/z ranges 130-160 (**Fig. 4a**), 310-340 (**Fig. 4b**) and 450-500 (**Fig. 4c**). It is found that the $Ce_{0.01}Mn$ sample displayed only Ce-containing secondary ions

with one Ce atom. This suggests that the surface of this sample is dominated by isolated monomeric species CeO_x [61]. On the other hand, for $Ce_{0.1}Mn$, the Ce-containing fragments with two ($Ce_2O_3^+$) and three Ce atoms ($Ce_3O_4^+$ and $Ce_3O_5^+$) are also observed in addition to CeO_x. Among the Ce and Mn related (±) secondary ions reported in **Table S1** several secondary ions $Ce_xMn_yO_zH_w^{+/-}$ reveal the presence of Ce-O-Mn interactions. As an example, the ToF-SIMS spectra in (+) mode in the 200-220 m/z range for calcined $Ce_{0.01}Mn$ and $Ce_{0.01}Mn$ shown in **Fig. 5a** and **Fig. 5b** exhibit secondary ions at m/z = 211 and 212 assigned to $CeMnO^+$ and $CeMnOH^+$, respectively, which indicates intimate interaction between Mn and Ce. Comparison of secondary ion intensity $CeOMn^+/(Ce^+ + Mn^+)$ ratios indicates that the amount of Ce-O-Mn interactions increases after calcination. Interestingly, the secondary ion intensity CeO^+/Ce^+ ratio decreases strongly upon calcination which might suggest a significant lowering of the Ce^{3+}/Ce^{4+} atomic ratio. In addition, the identification of KNa^+ as well as K_2NaMnO^+ and $K_2NaMnOH^+$ as secondary ions provides direct evidence of a close interaction between potassium and sodium. For $Ce_{0.01}Mn$-400, the presence of numerous Mn-O-Ce interactions leading to asymmetric oxygen/vacancy sites [62-65] along with a significant decrease of the secondary ion intensity CeO^+/Ce^+ ratio are believed to improve the catalytic performance in HCHO oxidation.

3.2. Catalytic activity

The conversion of 100 ppmv of HCHO into CO_2 as a function of temperature is displayed over the calcined Mn-B and $Ce_{0.01}Mn$ (**Fig. 6a**) and $Ce_{0.1}Mn$ (**Fig. 6b**) at a GHSV of 60 $L/(g_{cat}.h)$. T_{10}, T_{50} and T_{90} (corresponding to 10 %, 50 % and 90 % HCHO conversion) summarized in **Table 5** have been used to characterize the catalyst activity. Irrespective of the Ce/Mn ratio, it is found that the activity increases as the temperature of calcination increases. Among the different catalysts, $Ce_{0.01}Mn$-400 exhibits the best catalytic activity whith T_{50} and T_{90} of 50 °C and 73 °C, respectively. Note that the T_{50} of 50 °C is close to values reported in literature for the most active MnO_2 based catalysts as shown in **Table S2**.

As the effect of relative humidity on HCHO removal represents a key factor in catalytic performance assessment, experiments consisting in submitting the Ce_xMn-400 catalysts to 100 ppm of formaldehyde in flowing air with different water content (%RH: 0; 50 and 75) in three successive steps (the catalyst is kept in static reactive gas mixture between each step) have been carried out on the Ce_xMn-400 catalysts. **Fig. 7a** shows HCHO elimination and HCHO conversion into CO_2 and as a function of time on stream at 50 °C (corresponding to 50 % HCHO conversion over $Ce_{0.01}Mn$-400 based on the light-off curve result) over the calcined Ce_xMn catalysts. It is observed a slight decrease of the HCHO conversion into CO_2 over time in dry air for the $Ce_{0.01}Mn$-400 catalyst. However, the initial HCHO conversion is rapidly restored after water addition (50 %RH) to keep stable over time at 75 %RH. Conversely, the HCHO elimination close to 100 % at the beginning of each step decreases quite linearly to get final values of 75 % (%RH: 0; 50) and a stabilized value of about 60 % at 75 %RH. In any case, the higher HCHO elimination as compared to HCHO conversion into CO_2 indicates that part of HCHO is retained on the catalytic surface to stabilize at around 10% at 75 %RH. For $Ce_{0.1}Mn$-400 (**Fig. 7b**), the HCHO elimination also decreases rapidly at 0 %RH along with HCHO conversion into CO_2. When adding water, it is observed that the HCHO conversion into CO_2 remains stable after an induction period which decreases with increasing water content to reach a value of about 30 %. Additionally, the HCHO elimination increases over time to reach 50% at the end of the experiment which indicates that the retained quantity of HCHO on the catalyst amounts to 20%. Compared to $Ce_{0.01}Mn$-400, the two-fold increase of retained HCHO can be linked mainly to the difference in specific surface area of the catalysts.

To better apprehend the scheme of HCHO oxidation on the Ce modified birnessites, ATR-FTIR spectroscopy has been used to detect adsorbed species on the used catalysts. As shown in **Fig. 8** absorption bands at 1568, 1480, 1373, 1320 cm^{-1} have been observed on the surface of both catalysts. The bands at 1373 (δ(CH)) and 1565 cm^{-1} ($\nu_{as}(COO^-)$) can be attributed to

formate species [66] while the band at 1320 cm^{-1} (ν_s(COO)) is ascribed to carbonate adsorbed species [24]. The band located at about 1480 cm^{-1} can be due to the presence of dioxymethylene (DOM) species [33]. The bands observed at 1620 cm^{-1} and ~ 3180 cm^{-1} are consistent with the bending and stretching vibration bands of O-H for adsorbed water. The low amount of partially oxidized adsorbed species over both catalysts is in line with a good activity in HCHO oxidation. accumulation of partially oxidized species over $Ce_{0.01}Mn$-400 is in line with a better activity in HCHO oxidation. A synergetic oxidation mechanism of active oxygen and hydroxyl can account for such results. As OH promotes formate formation, active oxygen promotes formate oxidation step. The introduction of water in the reactive gas mixture can generate surface hydroxyl groups active towards formate oxidation which can be regenerated considering the reaction between H_2O from the feed and surface oxygen (O_2^-, $O^- + H_2O$ -> 2 –OH) [67,68]. **Fig. 9a** shows the superposition of the XRD patterns of the as-synthesized and used $Ce_{0.01}Mn$ catalyst in order to detect some structural changes after the stability test. The XRD patterns are superimposable except the low angle peak (001) which shifts after reaction to a higher 2θ value indicating an expansion of the interlayer spacing from 6.75 Å to 6.91 Å (**Fig. 9b**) without however recovering the initial value of the as-synthesized catalyst of 7.32 Å.

3.3. Role of temperature of calcination throughout the preparation of Ce modified birnessite-like MnO_2

Ce modified birnessite-like MnO_2 (Ce/Mn = 0.01; 0.1) have been successfully synthesized at ambient pressure and temperature through an easy redox-precipitation method involving $KMnO_4$ as oxidant and sodium lactate as reductant in the presence of cerium(III) nitrate. It has been found that Ce-coprecipitation greatly affects the final properties of the samples in terms of structural and textural properties. It has been observed a reduction of the mean crystallite size and an increase of the specific area by factors 3 and 6 by increasing the Ce/Mn ratio as

compared to that of the Ce free birnessite. HRTEM show that addition of Ce has high impact on the lateral layer size (a-b plane) of the particles which decreases markedly in the presence of Ce. Ce^{4+} sorptions during mineral formation on the vacancy sites disrupt layer formation. It is speculated that Ce^{4+} ions form inner-sphere sorption complexes above/below the vacancy sites as Mn^{4+} substitution by Ce^{4+} into octahedral sites in the MnO_2 layer seems unlikely due to the large size difference between Ce^{4+} ionic radius (97 pm) and those of Mn(III) of 58 pm or Mn(IV) of 53 pm.

It is observed that the catalytic activity for HCHO oxidation into CO_2 increases with Ce with an optimum Ce/Mn atomic ratio of 0.01 as the temperature of calcination increased. It follows that the highest HCHO conversion is obtained for the $Ce_{0.01}Mn$ catalyst calcined at 400 °C. For all fresh synthesized samples, it is shown that their compositions can be tuned by selecting the temperature of calcination through the occurrence of dehydration, dehydroxylation and oxygen departure processes which take place one after the other as the temperature of calcination increases. Based on these considerations, it is noted that the temperature of calcination at 400 °C affects greatly the final properties of the Ce modified birnessite-like MnO_2 catalysts particularly in terms of surface Mn^{3+}/Mn^{4+} ratios, Mn^{3+} distribution and $Ce^{4+/3+}/Mn^{4+/3+}$ interactions at the outermost layers. Indeed, at 400 °C, the high content of Mn^{3+} resulting from the reduction of Mn^{4+} layer is consistent with an enrichment of oxygen vacancies as these two entities are closely related due to charge compensating effect. Additionally, the possibility of migration of these Mn^{3+} species into the interlayer spacing might result in formation of cationic vacancies Vm.

In summary, the beneficial effect of the heating treatment at 400 °C is clarified in **scheme 1** assuming the well-recognized “active oxygen assisted pathway” and “hydroxyl assisted pathway” for HCHO total oxidation reaction in dry and moist air, respectively. In dry air, the HCHO oxidation follows the formate decomposition route (HCHO -> $(CH_2)O_2$ -> HCO_2^- ->

CO -> CO_2) [20] in line with the detection of adsorbed dioximethylene and formate species. By opposition, in the presence of moist air, HCHO oxidation follows a different pathway involving reaction between surface hydroxyls and formate following the pathway: HCHO -> HCO_2^- + OH° -> CO_2 + H_2O [69]. Regardless of the pathway under concern, it is expected to get advantage of the creation of asymmetric oxygen vacancy sites (Ce-□-Mn) at the outermost surface of the catalyst which have been previously recognized as intrinsic active centers in various redox reactions [62]. Formation of such new sites allow to activate O_2 more easily facilitating the formation of active oxygen species enable to oxidize formate species in a more efficient way. When regarding the "hydroxyl assisted pathway" these new active centers have also been believed to assist the dissociation of water more easily to regenerate the hydroxyls at the surface.

4. Conclusion

Cerium modified birnessite-like MnO_2 with low Ce/Mn ratios (0.01; 0.1) were prepared from a simple, fast and inexpensive redox reaction using permangante potassium and sodium lactate at ambient with addition of cerium nitrate and further calcined at different temperatures (200 °C - 400 °C). Ce-coprecipitation allowed to get solids with low crystallite size and high surface area due to Ce which acted as a particle growth inhibiter. The calcination temperature impacted significantly the physico-chemical properties of the Ce-coprecipitated samples. Our findings showed a decrease of the adsorbed/interspaced water and structural HO content and conversely an increase of the surface Mn^{3+}/Mn^{4+} ratio along with a $^{TC}Mn^{3+}$ fraction enrichment for $Ce_{0.01}Mn$ calcined at 400°C. More importantly, the density of Mn-O-Ce linkages at the outermost layers of the catalysts enhanced largely by calcination with increasing the temperature while the secondary ion intensity CeO^+/Ce^+ ratio decreased concomitantly. The enhancement of asymetric oygen vacancies appears as a key factor governing the high catalytic activity of the $Ce_{0.01}Mn$-400 catalyst by promoting O_2 dissociation, formation of activated oxygen species and facilitating surface oxygen mobility to oxidize more efficiently the reaction intermediates such as formate, dimethyloxide and carbonates in HCHO oxidation. Numerous active oxygen and formation of active OH groups by adding water in the feed allows also to get a very active and stable catalyst for HCHO oxidation in moist air which is a prerequiste for a possible industrial application.

Acknowledgments

This research is supported by a European Program INTERREG V France-Wallonie-Flanders (FEDER) (DepollutAir). The Chevreul Institute is thanked for its help in the development of this work through the ARCHI-CM project supported by the "Ministère de l'Enseignement Supérieur de la Recherche et de l'Innovation", the region "Hauts-de-France", the ERDF program of the European Union and the "Métropole Européenne de Lille". The authors thank Christine Lancelot, Olivier Gardoll, Pardis Simon, Laurence Burylo and Jean-Charles Morin for their contribution in TEM, H_2-TPR, XPS, XRD and ATR-FTIR measurements, respectively.

Captions

Fig. 1: TG curves of a) Mn-B, as-synthesized and calcined $Ce_{0.01}Mn$ and b) as-synthesized and calcined $Ce_{0.1}Mn$.

Fig. 2: XRD patterns of a) as-synthesized samples, b) calcined samples and c) zoom in the 10-20 ° 2θ range.

Fig.3: HAADF-HRSTEM images and bright field images of the as-syntesized $Ce_{0.1}Mn$ sample.

Fig. 4: ToF-SIMS positive ion spectra of $Ce_{0.01}Mn$-400 and $Ce_{0.1}Mn$-400 in the m/z range: a) 130-160, b) 310-340 and c) 450-500.

Fig. 5: ToF-SIMS positive ion spectra in the 200-220 m/z range of a) $Ce_{0.01}Mn$-400 and b) $Ce_{0.1}Mn$-400.

Fig. 6: Light off curves over a) Mn-B-400 and calcined $Ce_{0.01}Mn$ and b) calcined $Ce_{0.1}Mn$. HCHO = 100 ppm, O_2 = 20 %, N_2 balance, GHSV = 60 L/(g_{cat}.h) .

Fig. 7: Effect of RH on HCHO elimination and HCHO conversion over a) $Ce_{0.01}Mn$-400 and b) $Ce_{0.1}Mn$ -400. T = 50 °C, HCHO = 100 ppm, O_2 = 20%, N_2 balance, GHSV = 60 L/(g_{cat}.h).

Fig. 8: FTIR-ATR spectra of the used Ce_xMn-400 catalysts after stability tests

Fig. 9: a) XRD patterns of the as-synthesized and used $Ce_{0.01}Mn$-400 after stability test and b) zoom in the the 10-18 ° 2θ range.

Scheme 1: Mechanism of HCHO oxidation in dry and humid air over the $Ce_{0.01}Mn400$ catalyst.

References:

[1] M. Lippmann, G.D. Leikauf, Environmental toxicants: human exposures and their health effects, Fourth edition, Wiley, Hoboken, NJ, 2020.

[2] G.D. Leikauf, FORMALDEHYDE AND OTHER SATURATED ALDEHYDES, in: M. Lippmann, G.D. Leikauf (Eds.), Environmental Toxicants, human exposures and their health effects, Fourth edition, Wiley, 2020: pp. 555–626. https://doi.org/10.1002/9781119438922.ch16.

[3] S. Rong, P. Zhang, J. Wang, F. Liu, Y. Yang, G. Yang, S. Liu, Ultrathin manganese dioxide nanosheets for formaldehyde removal and regeneration performance, Chem. Engin. J. 306 (2016) 1172–1179. https://doi.org/10.1016/j.cej.2016.08.059.

[4] J.-P. Bellat, I. Bezverkhyy, G. Weber, S. Royer, R. Averlant, J.-M. Giraudon, J.-F. Lamonier, Capture of formaldehyde by adsorption on nanoporous materials, J. Hazard. Mater. 300 (2015) 711–717. https://doi.org/10.1016/j.jhazmat.2015.07.078.

[5] X. Feng, H. Liu, C. He, Z. Shen, T. Wang, Synergistic effects and mechanism of a non-thermal plasma catalysis system in volatile organic compound removal: a review, Catal. Sci. Technol. 8 (2018) 936–954. https://doi.org/10.1039/C7CY01934C.

[6] X. Zhu, D.-L. Chang, X.-S. Li, Z.-G. Sun, X.-Q. Deng, A.-M. Zhu, Inherent rate constants and humidity impact factors of anatase TiO_2 film in photocatalytic removal of formaldehyde from air, Chem. Engin. J. 279 (2015) 897–903. https://doi.org/10.1016/j.cej.2015.05.095.

[7] X. Zhu, C. Jin, X.-S. Li, J.-L. Liu, Z.-G. Sun, C. Shi, X. Li, A.-M. Zhu, Photocatalytic Formaldehyde Oxidation over Plasmonic Au/TiO_2 under Visible Light: Moisture Indispensability and Light Enhancement, ACS Catal. 7 (2017) 6514–6524. https://doi.org/10.1021/acscatal.7b01658.

[8] J. Quiroz, J.-M. Giraudon, A. Gervasini, C. Dujardin, C. Lancelot, M. Trentesaux, J.-F. Lamonier, Total Oxidation of Formaldehyde over MnO_x-CeO_2 Catalysts: The Effect of Acid Treatment, ACS Catal. 5 (2015) 2260–2269. https://doi.org/10.1021/cs501879j.

[9] C. Ciotonea, R. Averlant, G. Rochard, A.-S. Mamede, J.-M. Giraudon, H. Alamdari, J.-F. Lamonier, S. Royer, A Simple and Green Procedure to Prepare Efficient Manganese Oxide Nanopowder for the Low Temperature Removal of Formaldehyde, ChemCatChem. 9 (2017) 2366–2376. https://doi.org/10.1002/cctc.201700199.

[10] J. Quiroz Torres, S. Royer, J.-P. Bellat, J.-M. Giraudon, J.-F. Lamonier, Formaldehyde: Catalytic Oxidation as a Promising Soft Way of Elimination, ChemSusChem. 6 (2013) 578–592. https://doi.org/10.1002/cssc.201200809.

[11] L. Nie, J. Yu, M. Jaroniec, F.F. Tao, Room-temperature catalytic oxidation of formaldehyde on catalysts, Catal. Sci. Technol. 6 (2016) 3649–3669. https://doi.org/10.1039/C6CY00062B.

[12] Y. Boyjoo, G. Rochard, J.-M. Giraudon, J. Liu, J.-F. Lamonier, Mesoporous MnO_2 hollow spheres for enhanced catalytic oxidation of formaldehyde, Sustain. Mater. Technol. 20 (2019) e00091. https://doi.org/10.1016/j.susmat.2018.e00091.

[13] C. Zhang, F. Liu, Y. Zhai, H. Ariga, N. Yi, Y. Liu, K. Asakura, M. Flytzani-Stephanopoulos, H. He, Alkali-Metal-Promoted Pt/TiO2 Opens a More Efficient Pathway to Formaldehyde Oxidation at Ambient Temperatures, Angew. Chem. 124 (2012) 9766–9770. https://doi.org/10.1002/ange.201202034.

[14] C. Zhang, Y. Li, Y. Wang, H. He, Sodium-Promoted Pd/TiO_2 for Catalytic Oxidation of Formaldehyde at Ambient Temperature, Environ. Sci. Technol. 48 (2014) 5816–5822. https://doi.org/10.1021/es4056627.

[15] B. Bai, Q. Qiao, J. Li, J. Hao, Progress in research on catalysts for catalytic oxidation of formaldehyde, Chinese J. Catal. 37 (2016) 102–122. https://doi.org/10.1016/S1872-2067(15) 61007-5.

[16] S. Zhu, J. Wang, L. Nie, Progress of Catalytic Oxidation of Formaldehyde over Manganese Oxides, ChemistrySelect. 4 (2019) 12085–12098. https://doi.org/10.1002/slct.201902701.

[17] J. Quiroz -Torres, R. Averlant, J.-M. Giraudon, J.-F. Lamonier, Mesoporous manganese oxide catalysts for formaldehyde removal: influence of the cerium incorporation, in: Studies in Surface Science and Catalysis, Elsevier, 2010: pp. 517–520. https://doi.org/10.1016/S0167-2991(10) 75098-9.

[18] J. Wang, D. Li, P. Li, P. Zhang, Q. Xu, J. Yu, Layered manganese oxides for formaldehyde-oxidation at room temperature: the effect of interlayer cations, RSC Adv. 5 (2015) 100434–100442. https://doi.org/10.1039/C5RA17018D.

[19] Y. Sekine, Oxidative decomposition of formaldehyde by metal oxides at room temperature, Atmos. Environ. 36 (2002) 5543–5547. https://doi.org/10.1016/S1352-2310(02)00670-2.

[20] L. Miao, J. Wang, P. Zhang, Review on manganese dioxide for catalytic oxidation of airborne formaldehyde, Appl. Surf. Sci. 466 (2019) 441–453. https://doi.org/10.1016/j.apsusc.2018.10.031.

[21] J. Gong, S. Rong, X. Wang, Y. Zhou, Critical review of catalytic degradation of formaldehyde via MnO_2: From the perspective of process intensification, J. Clea. Prod. 377 (2022) 134242. https://doi.org/10.1016/j.jclepro.2022.134242.

[22] R. Averlant, S. Royer, J.-M. Giraudon, J.-P. Bellat, I. Bezverkhyy, G. Weber, J.-F. Lamonier, Mesoporous Silica-Confined Manganese Oxide Nanoparticles as Highly Efficient Catalysts for the Low-Temperature Elimination of Formaldehyde, ChemCatChem. 6 (2014) 152–161. https://doi.org/10.1002/cctc.201300544.

[23] J. Zhang, Y. Li, L. Wang, C. Zhang, H. He, Catalytic oxidation of formaldehyde over manganese oxides with different crystal structures, Catal. Sci. Technol. 5 (2015) 2305–2313. https://doi.org/10.1039/C4CY01461H.

[24] J. Wang, G. Zhang, P. Zhang, Layered birnessite-type MnO_2 with surface pits for enhanced catalytic formaldehyde oxidation activity, J. Mater. Chem. A. 5 (2017) 5719–5725. https://doi.org/10.1039/C6TA09793F.

[25] S. Selvakumar, N. Nuns, M. Trentesaux, V.S. Batra, J.-M. Giraudon, J.-F. Lamonier, Reaction of formaldehyde over birnessite catalyst: A combined XPS and ToF-SIMS study, Appl. Catal. B: Environ. 223 (2018) 192–200. https://doi.org/10.1016/j.apcatb.2017.05.029.

[26] Y. Xu, J. Dhainaut, G. Rochard, J.-P. Dacquin, A.-S. Mamede, J.-M. Giraudon, J.-F. Lamonier, H. Zhang, S. Royer, Hierarchical porous ε-MnO_2 from perovskite precursor: Application to the formaldehyde total oxidation, Chem. Engin. J. 388 (2020) 124146. https://doi.org/10.1016/j.cej.2020.124146.

[27] Z. Han, C. Wang, X. Zou, T. Chen, S. Dong, Y. Zhao, J. Xie, H. Liu, Diatomite-supported birnessite–type MnO_2 catalytic oxidation of formaldehyde: Preparation, performance and mechanism, Appl. Surf. Sci. 502 (2020) 144201. https://doi.org/10.1016/j.apsusc.2019.144201.

[28] S.-B. Do, S.-E. Lee, T.-O. Kim, Oxidative decomposition with PEG-MnO_2 catalyst for removal of formaldehyde: Chemical aspects on HCHO oxidation mechanism, Appl. Surf. Sci. 598 (2022) 153773. https://doi.org/10.1016/j.apsusc.2022.153773.

[29] E. Silvester, A. Manceau, V.A. Drits, Structure of synthetic monoclinic Na-rich birnessite and hexagonal birnessite; II, Results from chemical studies and EXAFS spectroscopy, Am. Mineral. 82 (1997) 962–978. https://doi.org/10.2138/am-1997-9-1013.

[30] A.-C. Gaillot, Caractérisation structurale de la birnessite : Influence du protocole de synthèse, Docteur de l'Université Joseph Fourier – Grenoble I. (2002) 1–392.

[31] B. Lanson, V.A. Drits, Q. Feng, A. Manceau, Structure of synthetic Na-birnessite: Evidence for a triclinic one-layer unit cell, Am. Mineral. 87 (2002) 1662–1671. https://doi.org/10.2138/am-2002-11-1215.

[32] M.A. Cheney, P.K. Bhowmik, S. Qian, S.W. Joo, W. Hou, J.M. Okoh, A New Method of Synthesizing Black Birnessite Nanoparticles: From Brown to Black Birnessite with Nanostructures, J. Nanomater. 2008 (2008) 1–8. https://doi.org/10.1155/2008/763706.

[33] J. Wang, J. Li, C. Jiang, P. Zhou, P. Zhang, J. Yu, The effect of manganese vacancy in birnessite-type MnO_2 on room-temperature oxidation of formaldehyde in air, Appl. Catal. B: Environ. 204 (2017) 147–155. https://doi.org/10.1016/j.apcatb.2016.11.036.

[34] S. Rong, K. Li, P. Zhang, F. Liu, J. Zhang, Potassium associated manganese vacancy in birnessite-type manganese dioxide for airborne formaldehyde oxidation, Catal. Sci. Technol. 8 (2018) 1799–1812. https://doi.org/10.1039/C7CY02121F.

[35] J. Ji, X. Lu, C. Chen, M. He, H. Huang, Potassium-modulated δ-MnO_2 as robust catalysts for formaldehyde oxidation at room temperature, Appl. Catal. B: Environ. 260 (2020) 118210. https://doi.org/10.1016/j.apcatb.2019.118210.

[36] Y. Lou, X.-M. Cao, J. Lan, L. Wang, Q. Dai, Y. Guo, J. Ma, Z. Zhao, Y. Guo, P. Hu, G. Lu, Ultralow-temperature CO oxidation on an In_2O_3–Co_3O_4 catalyst: a strategy to tune CO adsorption strength and oxygen activation simultaneously, Chem. Commun. 50 (2014) 6835–6838. https://doi.org/10.1039/C4CC00036F.

[37] S. Guan, Q. Huang, J. Ma, W. Li, A.T. Ogunbiyi, Z. Zhou, K. Chen, Q. Zhang, HCHO Removal by MnO_2(x)–CeO_2 : Influence of the Synergistic Effect on the Catalytic Activity, Ind. Eng. Chem. Res. 59 (2020) 596–608. https://doi.org/10.1021/acs.iecr.9b05191.

[38] X. Liu, J. Lu, K. Qian, W. Huang, M. Luo, A comparative study of formaldehyde and carbon monoxide complete oxidation on MnO_x-CeO_2 catalysts, J. Rare Earths. 27 (2009) 418–424. https://doi.org/10.1016/S1002-0721(08)60263-X.

[39] L. Zhu, J. Wang, S. Rong, H. Wang, P. Zhang, Cerium modified birnessite-type MnO_2 for gaseous formaldehyde oxidation at low temperature, Appl. Catal. B: Environ. 211 (2017) 212–221. https://doi.org/10.1016/j.apcatb.2017.04.025.

[40] J. Wang, P. Zhang, J. Li, C. Jiang, R. Yunus, J. Kim, Room-Temperature Oxidation of Formaldehyde by Layered Manganese Oxide: Effect of Water, Environ. Sci. Technol. 49 (2015) 12372–12379. https://doi.org/10.1021/acs.est.5b02085.

[41] C. Mang, J. Luo, P. Cao, X. Zhang, M. Rao, G. Li, T. Jiang, Importance of water content in birnessite-type MnO_2 catalysts for HCHO oxidation: Mechanistic details and DFT analysis, Chemosphere. 287 (2022) 132293. https://doi.org/10.1016/j.chemosphere.2021.132293.

[42] M. Händel, T. Rennert, K.U. Totsche, A simple method to synthesize birnessite at ambient pressure and temperature, Geoderma. 193–194 (2013) 117–121. https://doi.org/10.1016/j.geoderma.2012.09.002.

[43] M.C. Biesinger, B.P. Payne, A.P. Grosvenor, L.W.M. Lau, A.R. Gerson, R.St.C. Smart, Resolving surface chemical states in XPS analysis of first row transition metals, oxides and hydroxides: Cr, Mn, Fe, Co and Ni, Appl. Surf. Sci. 257 (2011) 2717–2730. https://doi.org/10.1016/j.apsusc.2010.10.051.

[44] N. Birkner, A. Navrotsky, Thermodynamics of manganese oxides: Sodium, potassium, and calcium birnessite and cryptomelane, Proc. Natl. Acad. Sci. USA. 114 (2017) E1046–E1053. https://doi.org/10.1073/pnas.1620427114.

[45] C.L. Lopano, P.J. Heaney, J.E. Post, J. Hanson, S. Komarneni, Time-resolved structural analysis of K- and Ba-exchange reactions with synthetic Na-birnessite using synchrotron X-ray diffraction, Am. Mineral. 92 (2007) 380–387. https://doi.org/10.2138/am.2007.2242.

[46] 0A. Putnis, Mineral replacement reactions: from macroscopic observations to microscopic mechanisms, Mineral. Mag. 66 (2002) 689–708. https://doi.org/10.1180/0026461026650056.

[47] A.-C. Gaillot, B. Lanson, V.A. Drits, Structure of Birnessite Obtained from Decomposition of Permanganate under Soft Hydrothermal Conditions. 1. Chemical and Structural Evolution as a Function of Temperature, Chem. Mater. 17 (2005) 2959–2975. https://doi.org/10.1021/cm0500152.

[48] R. Chen, P. Zavalij, M.S. Whittingham, Hydrothermal Synthesis and Characterization of K_xMnO_2•yH_2O, Chem.Mater. 8 (1996) 1275–1280. https://doi.org/10.1021/cm950550+.

[49] S. Grangeon, A. Fernandez-Martinez, F. Warmont, A. Gloter, N. Marty, A. Poulain, B. Lanson, Cryptomelane formation from nanocrystalline vernadite precursor: a high energy X-

ray scattering and transmission electron microscopy perspective on reaction mechanisms, Gechem. Trans.16 (2015). https://doi.org/10.1186/s12932-015-0028-y.

[50] M.A. Cheney, P.K. Bhowmik, S. Moriuchi, M. Villalobos, S. Qian, S.W. Joo, The Effect of Stirring on the Morphology of Birnessite Nanoparticles, J. Nanomater. 2008 (2008) 1–9. https://doi.org/10.1155/2008/168716.

[51] S.H. Kim, S.J. Kim, S.M. Oh, Preparation of Layered MnO_2 via Thermal Decomposition of $KMnO_4$ and Its Electrochemical Characterizations, Chem. Mater. 11 (1999) 557–563. https://doi.org/10.1021/cm9801643.

[52] A.-C. Gaillot, D. Flot, V.A. Drits, A. Manceau, M. Burghammer, B. Lanson, Structure of Synthetic K-rich Birnessite Obtained by High-Temperature Decomposition of $KMnO_4$. I. Two-Layer Polytype from 800°C Experiment, Chem. Mater. 15 (2003) 4666–4678. https://doi.org/10.1021/cm021733g.

[53] V.A. Drits, E. Silvester, A.I. Gorshkov, A. Manceau, Structure of synthetic monoclinic Na-rich birnessite and hexagonal birnessite: I. Results from X-ray diffraction and selected-area electron diffraction. Am. Mineral. 82 (1997) 946–961. https://doi.org/10.2138/am-1997-9-1012.

[54] S. Grangeon, A. Fernandez-Martinez, F. Claret, N. Marty, C. Tournassat, F. Warmont, A. Gloter, In-situ determination of the kinetics and mechanisms of nickel adsorption by nanocrystalline vernadite, Chem. Geol. 459 (2017) 24–31. https://doi.org/10.1016/j.chemgeo.2017.03.035.

[55] S. Lee, H. Xu, W. Xu, X. Sun, The structure and crystal chemistry of vernadite in ferromanganese crusts, Acta. Crystallogr. B. Struct. Sci. Cryst. Eng. Mater. 75 (2019) 591–598. https://doi.org/10.1107/S2052520619006528.

[56] S. Grangeon, B. Lanson, M. Lanson and A. Manceau, Crystal structure of Ni-sorbed synthetic vernadite: A powder X-ray diffraction study, Mineral. Mag. 72(6) (2008) 1279-1291, https://doi.org/10.1180/minmag.2008.072.6.1279.

[57] E.A. Johnson, J.E. Post, Water in the interlayer region of birnessite: Importance in cation exchange and structural stability, Am. Mineral. 91 (2006) 609–618. https://doi.org/10.2138/am.2006.2090.

[58] D.R. Mullins, S.H. Overbury, D.R. Huntley, Electron spectroscopy of single crystal and polycrystalline cerium oxide surfaces, Surf. Sci. 409 (1998) 307–319. https://doi.org/10.1016/S0039-6028(98)00257-X.

[59] H. Shen, J. Bu, W. Wang, C.Wu, Y. Cao, B. Zhang, Q.Zhang, H. Zhang, Insight into Ce Doping Induced Oxygen Vacancies over Ce-Doped MnO_2 Catalysts for Imine Synthesis, Chin. J. Chem. 38 (2020) 1353-1359. https://doi.org/10.1002/cjoc.202000155.

[60] L.-T. Weng, Advances in the surface characterization of heterogeneous catalysts using ToF-SIMS, Appl. Catal. A: Gen. 474 (2014) 203–210. https://doi.org/10.1016/j.apcata.2013.08.029.

[61] D.P. Debecker, B. Schimmoeller, M. Stoyanova, C. Poleunis, P. Bertrand, U. Rodemerck, E.M. Gaigneaux, Flame-made MoO_3/SiO_2–Al_2O_3 metathesis catalysts with highly

dispersed and highly active molybdate species, J. Catal. 277 (2011) 154–163. https://doi.org/10.1016/j.jcat.2010.11.003.

[62] K. Yu, L. Lou, S. Liu, W. Zhou, Asymmetric Oxygen Vacancies: the Intrinsic Redox Active Sites in Metal Oxide Catalysts, Adv. Sci. 7 (2020) 1901970. https://doi.org/10.1002/advs.201901970.

[63] G.E. Murgida, V. Ferrari, M.V. Ganduglia-Pirovano, A.M. Llois, Ordering of oxygen vacancies and excess charge localization in bulk ceria: A DFT + U study, Phys. Rev. B. 90 (2014) 115120. https://doi.org/10.1103/PhysRevB.90.115120.

[64] P. Zhang, H. Lu, Y. Zhou, L. Zhang, Z. Wu, S. Yang, H. Shi, Q. Zhu, Y. Chen, S. Dai, Mesoporous $MnCeO_x$ solid solutions for low temperature and selective oxidation of hydrocarbons, Nat Commun. 6 (2015) 8446. https://doi.org/10.1038/ncomms9446.

[65] S. Ramana, B.G. Rao, P. Venkataswamy, A. Rangaswamy, B.M. Reddy, Nanostructured Mn-doped ceria solid solutions for efficient oxidation of vanillyl alcohol, J. Mol. Catal. A: Chemical. 415 (2016) 113–121. https://doi.org/10.1016/j.molcata.2016.01.028.

[66] Y. Zhang, M. Chen, Z. Zhang, Z. Jiang, W. Shangguan, H. Einaga, Simultaneously catalytic decomposition of formaldehyde and ozone over manganese cerium oxides at room temperature: Promotional effect of relative humidity on the $MnCeO_x$ solid solution, Catal. Today. 327 (2019) 323–333. https://doi.org/10.1016/j.cattod.2018.04.027.

[67] B. Chen, X. Zhu, M. Crocker, Y. Wang, C. Shi, FeOx-supported gold catalysts for catalytic removal of formaldehyde at room temperature, Appl. Catal. B: Environ. 154–155 (2014) 73–81. https://doi.org/10.1016/j.apcatb.2014.02.009.

[68] B.-B. Chen, C. Shi, M. Crocker, Y. Wang, A.-M. Zhu, Catalytic removal of formaldehyde at room temperature over supported gold catalysts, Appl. Catal. B: Environ. 132–133 (2013) 245–255. https://doi.org/10.1016/j.apcatb.2012.11.028.

[69] X. Wang, Z. Rui, H. Jia, DFT study of formaldehyde oxidation on silver cluster by active oxygen and hydroxyl groups: Mechanism comparison and synergistic effect, Catal.Today 347 (2020) 124-133. https://doi.org/10.1016/j.cattod.2018.06.021.

Fig. 1

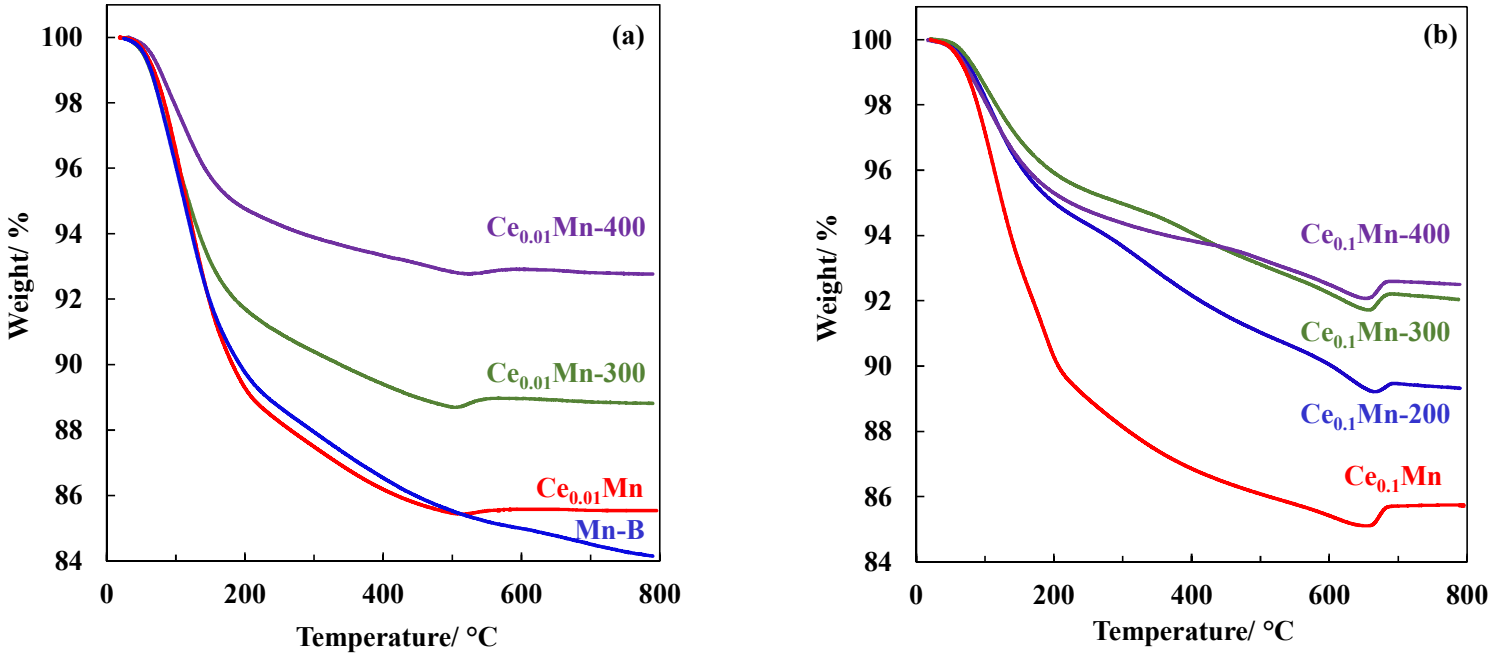
(a)
100
98
96
94
92
90
88
86
84
Weight/ %
0
200
400
600
800
Temperature/ °C
Ce0.01Mn-400
Ce0.01Mn-300
Ce0.01Mn
Mn-B
(b)
100
98
96
94
92
90
88
86
84
Weight/ %
0
200
400
600
800
Temperature/ °C
Ce0.1Mn-400
Ce0.1Mn-300
Ce0.1Mn-200
Ce0.1Mn

Fig. 2

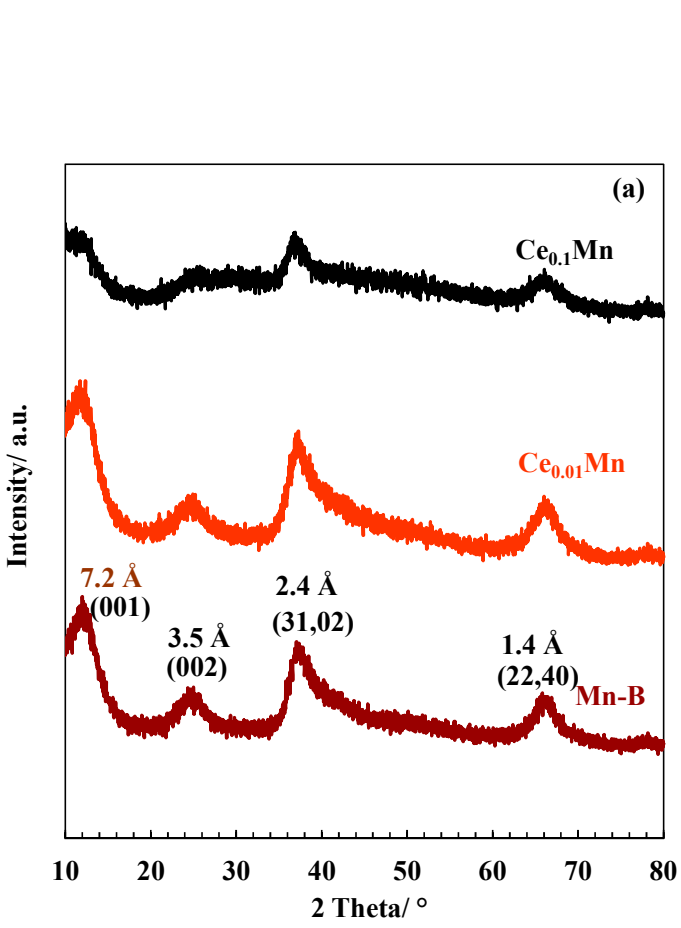
(a)
Ce0.1Mn
Ce0.01Mn
7.2 Å
(001)
3.5 Å
(002)
2.4 Å
(31,02)
1.4 Å
(22,40)
Mn-B
Intensity/ a.u.
10
20
30
40
50
60
70
80
2 Theta/ °

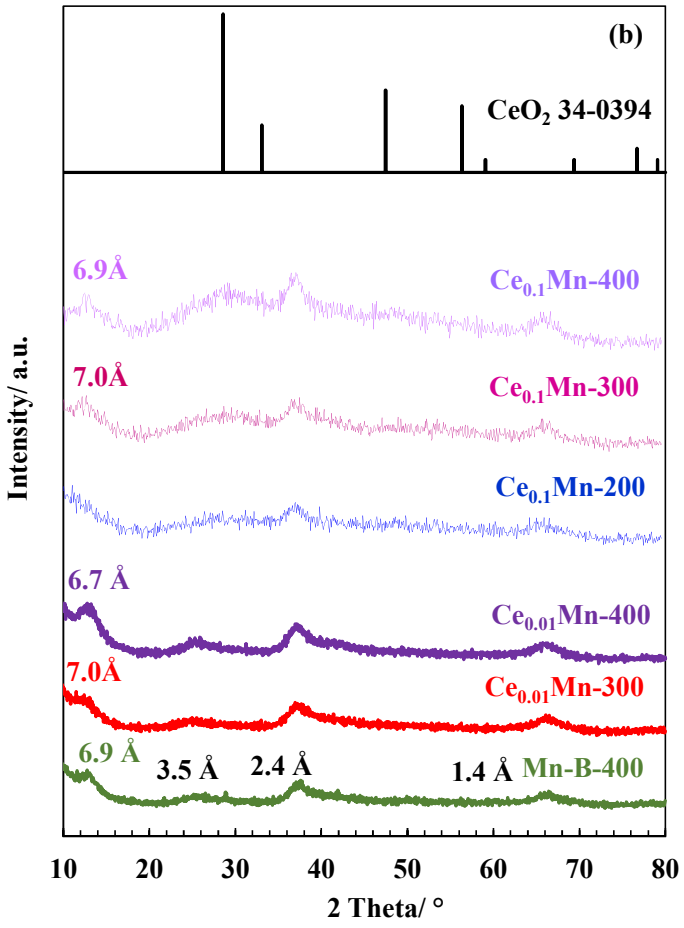
(b)
CeO2 34-0394
6.9Å
Ce0.1Mn-400
7.0Å
Ce0.1Mn-300
Ce0.1Mn-200
6.7 Å
Ce0.01Mn-400
7.0Å
Ce0.01Mn-300
6.9 Å
3.5 Å
2.4 Å
1.4 Å
Mn-B-400
Intensity/ a.u.
10
20
30
40
50
60
70
80
2 Theta/ °

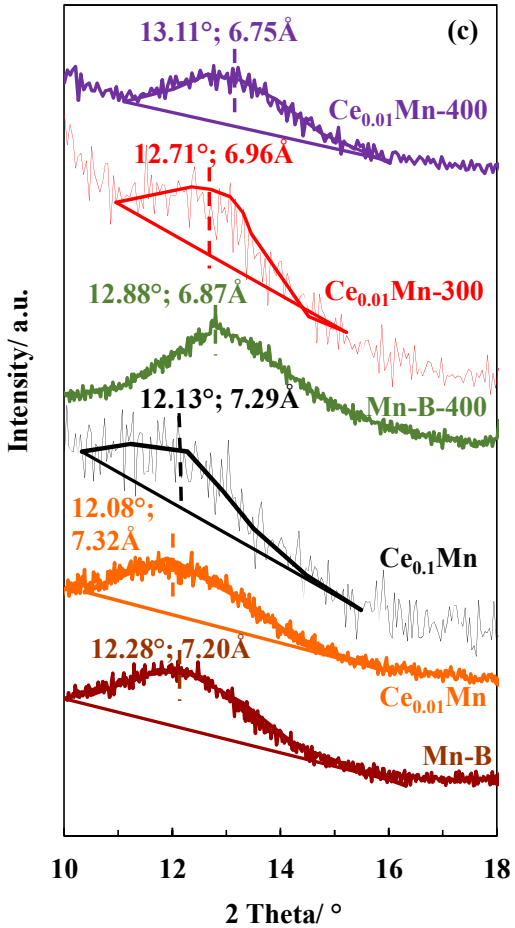
(c)
13.11°; 6.75Å
Ce0.01Mn-400
12.71°; 6.96Å
Ce0.01Mn-300
12.88°; 6.87Å
12.13°; 7.29Å
Mn-B-400
12.08°;
7.32Å
Ce0.1Mn
12.28°; 7.20Å
Ce0.01Mn
Mn-B
Intensity/ a.u.
10
12
14
16
18
2 Theta/ °

Fig. 3

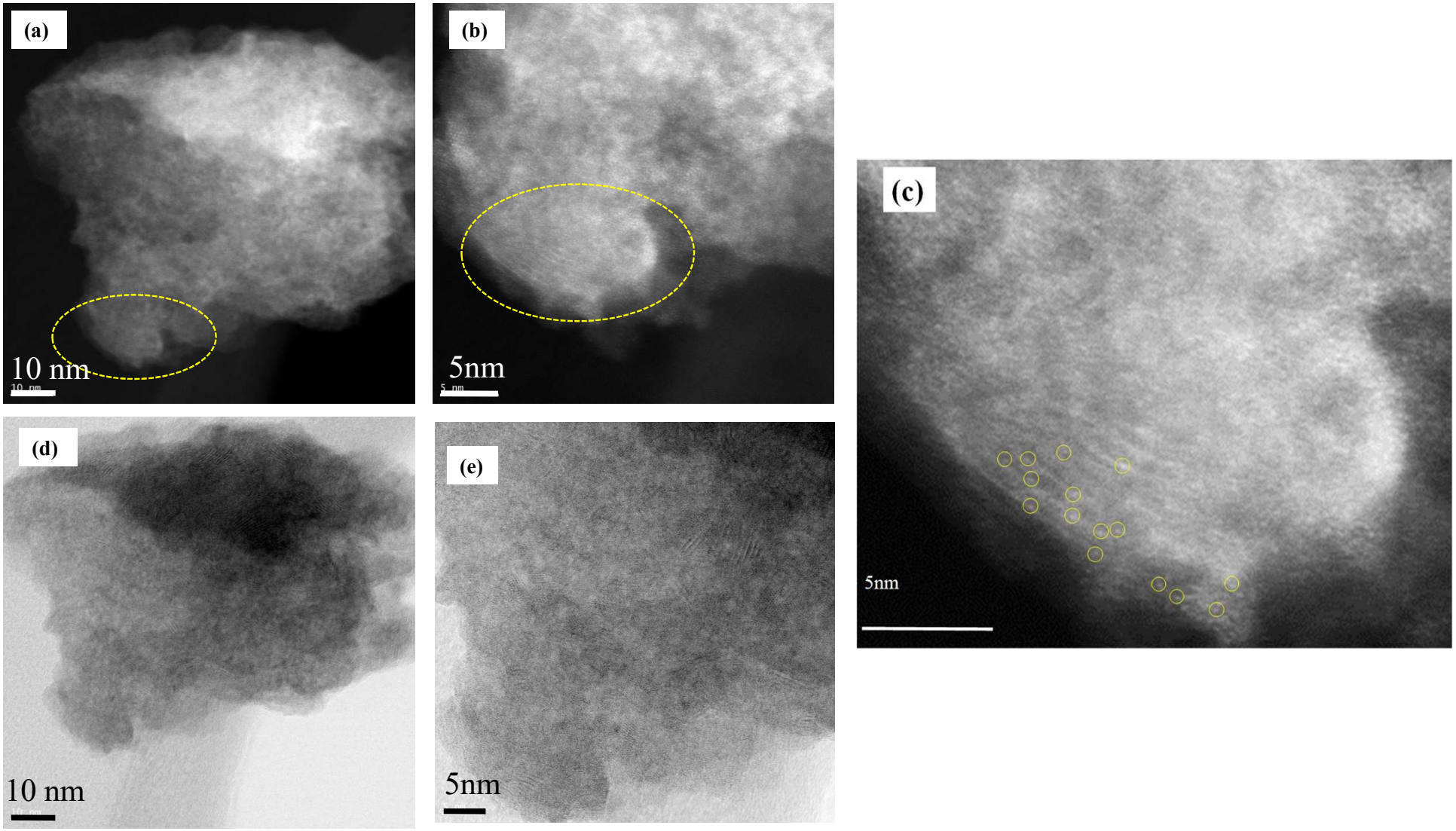

Fig. 4

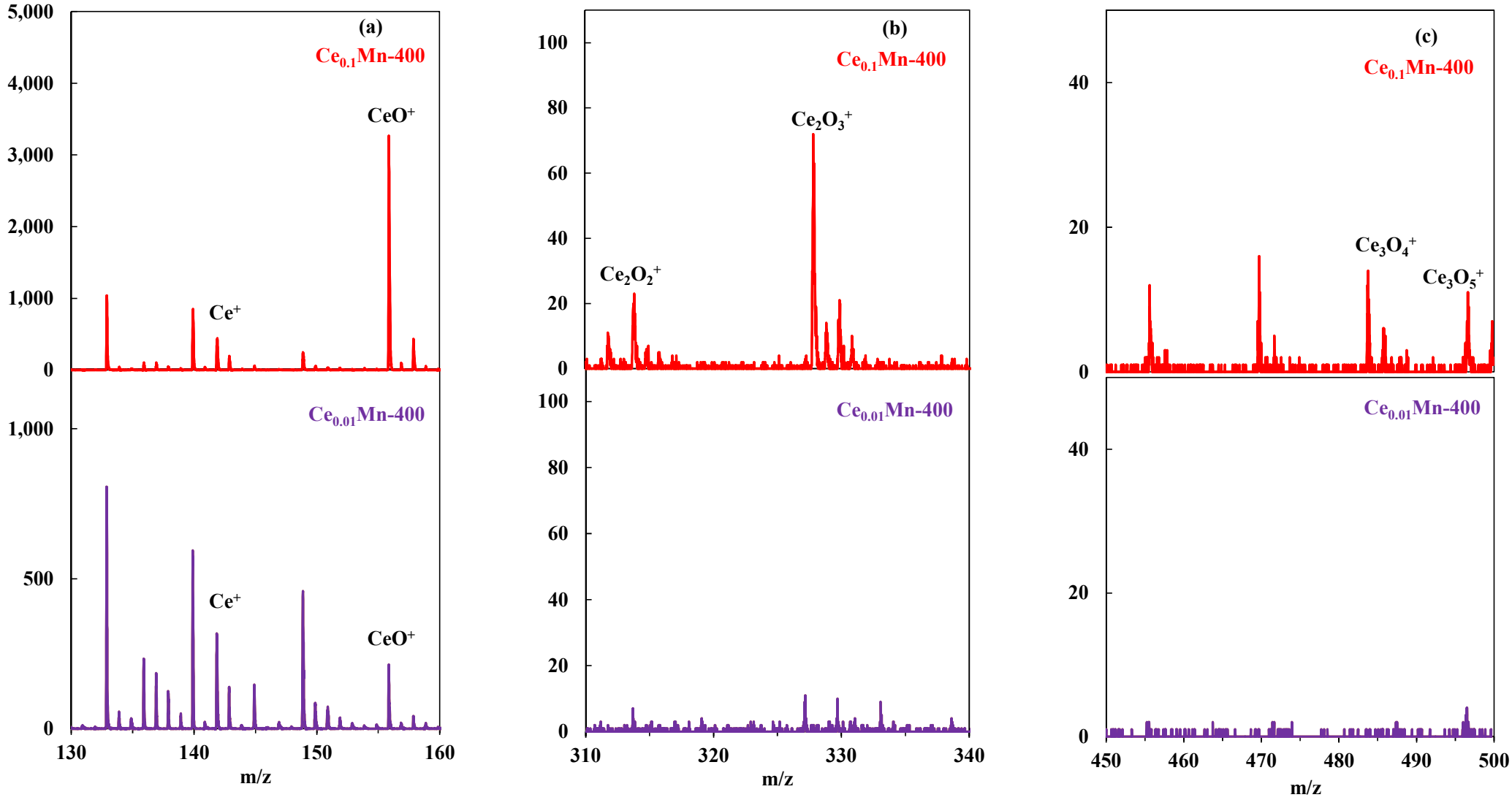
(a)
Ce0.1Mn-400
CeO+
Ce+
Ce0.01Mn-400
Ce+
CeO+
5,000
4,000
3,000
2,000
1,000
0
1,000
500
0
130
140
150
160
m/z
(b)
Ce0.1Mn-400
Ce2O3+
Ce2O2+
Ce0.01Mn-400
100
80
60
40
20
0
100
80
60
40
20
0
310
320
330
340
m/z
(c)
Ce0.1Mn-400
Ce3O4+
Ce3O5+
Ce0.01Mn-400
40
20
0
40
20
0
450
460
470
480
490
500
m/z

Fig. 5

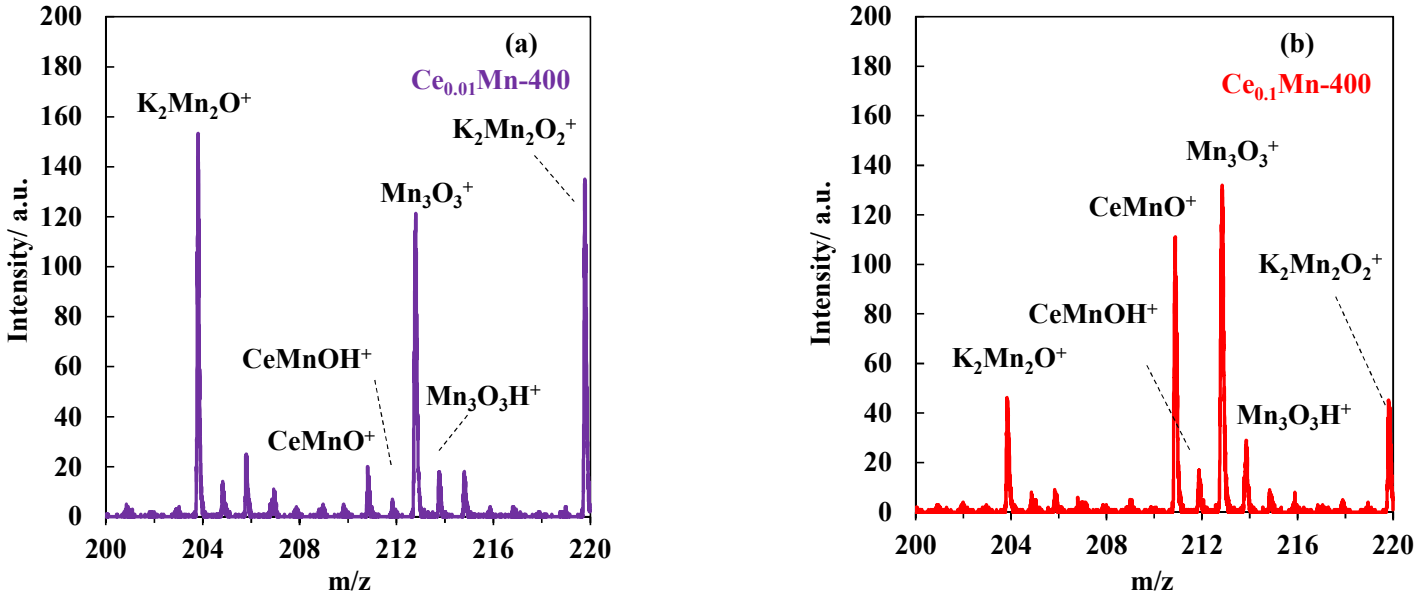
(a)
Ce0.01Mn-400
K2Mn2O+
K2Mn2O2+
Mn3O3+
CeMnOH+
CeMnO+
Mn3O3H+
Intensity/ a.u.
m/z
200
180
160
140
120
100
80
60
40
20
0
200
204
208
212
216
220
(b)
Ce0.1Mn-400
Mn3O3+
CeMnO+
K2Mn2O2+
CeMnOH+
K2Mn2O+
Mn3O3H+
Intensity/ a.u.
m/z

Fig. 6

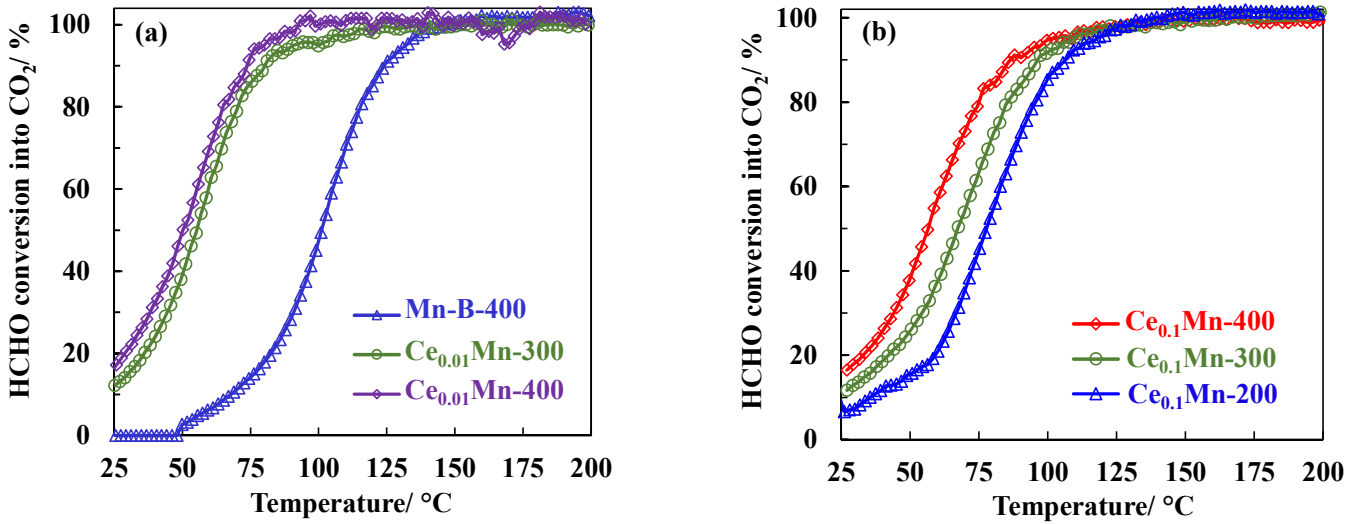
(a)
HCHO conversion into CO_2/ %
Temperature/ °C
Mn-B-400
$Ce_{0.01}$Mn-300
$Ce_{0.01}$Mn-400
(b)
HCHO conversion into CO_2/ %
Temperature/ °C
$Ce_{0.1}$Mn-400
$Ce_{0.1}$Mn-300
$Ce_{0.1}$Mn-200

Fig. 7

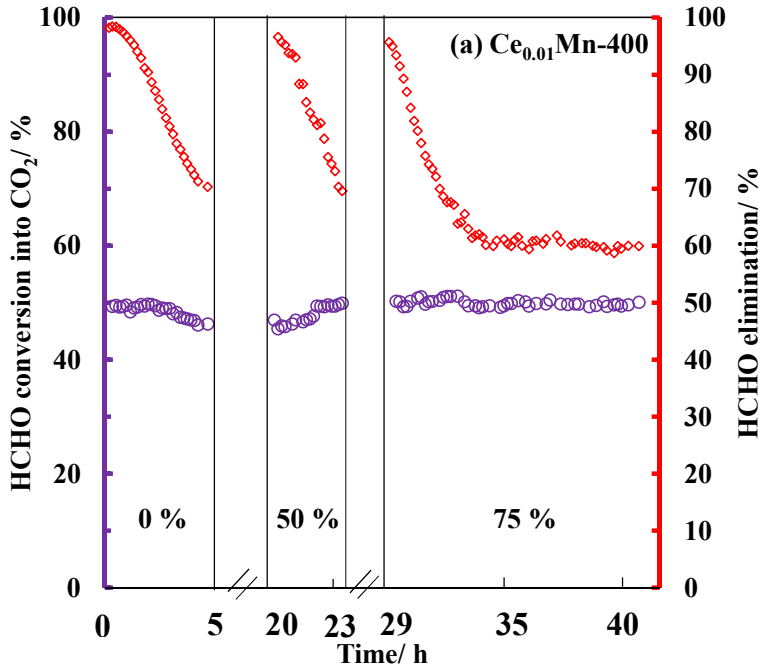
(a) $Ce_{0.01}Mn$-400
HCHO conversion into CO_2/ %
HCHO elimination/ %
Time/ h
0 %
50 %
75 %
0
5
20
23
29
35
40
0
20
40
60
80
100
0
10
20
30
40
50
60
70
80
90
100

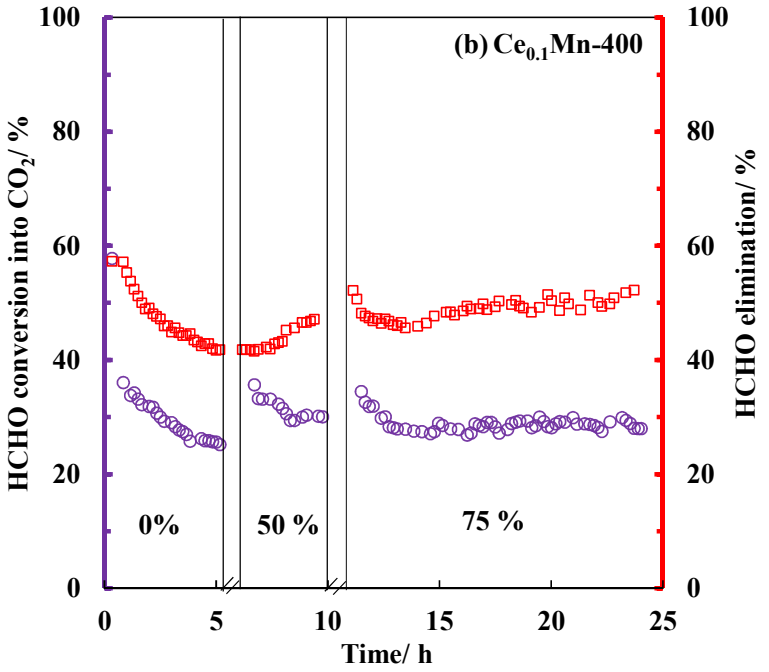
(b) $Ce_{0.1}Mn$-400
HCHO conversion into CO_2/ %
HCHO elimination/ %
Time/ h
0%
50 %
75 %
0
5
10
15
20
25
0
20
40
60
80
100
0
20
40
60
80
100

Fig. 8

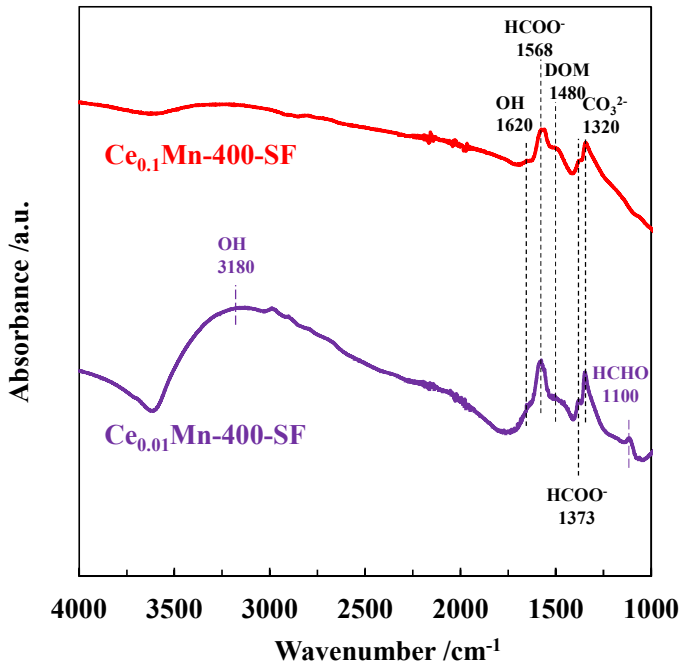
HCOO-
1568
DOM
1480
OH
1620
CO3 2-
1320
Ce0.1Mn-400-SF
OH
3180
HCHO
1100
Ce0.01Mn-400-SF
HCOO-
1373
Absorbance /a.u.
4000
3500
3000
2500
2000
1500
1000
Wavenumber /cm-1

Fig. 9

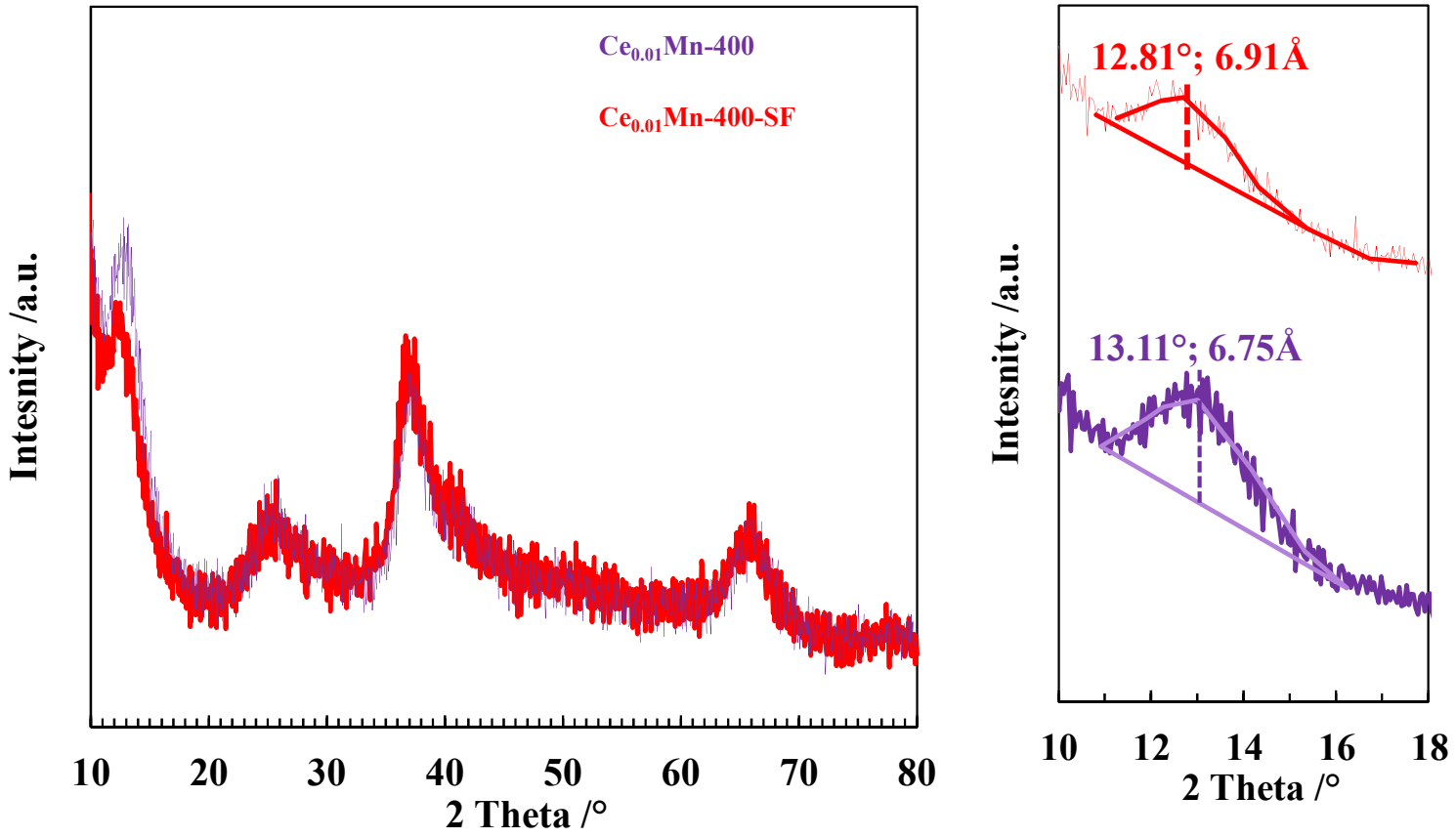
Ce0.01Mn-400
Ce0.01Mn-400-SF
Intesnity /a.u.
10
20
30
40
50
60
70
80
2 Theta /°
12.81°; 6.91Å
13.11°; 6.75Å
Intesnity /a.u.
10
12
14
16
18
2 Theta /°

Scheme 1

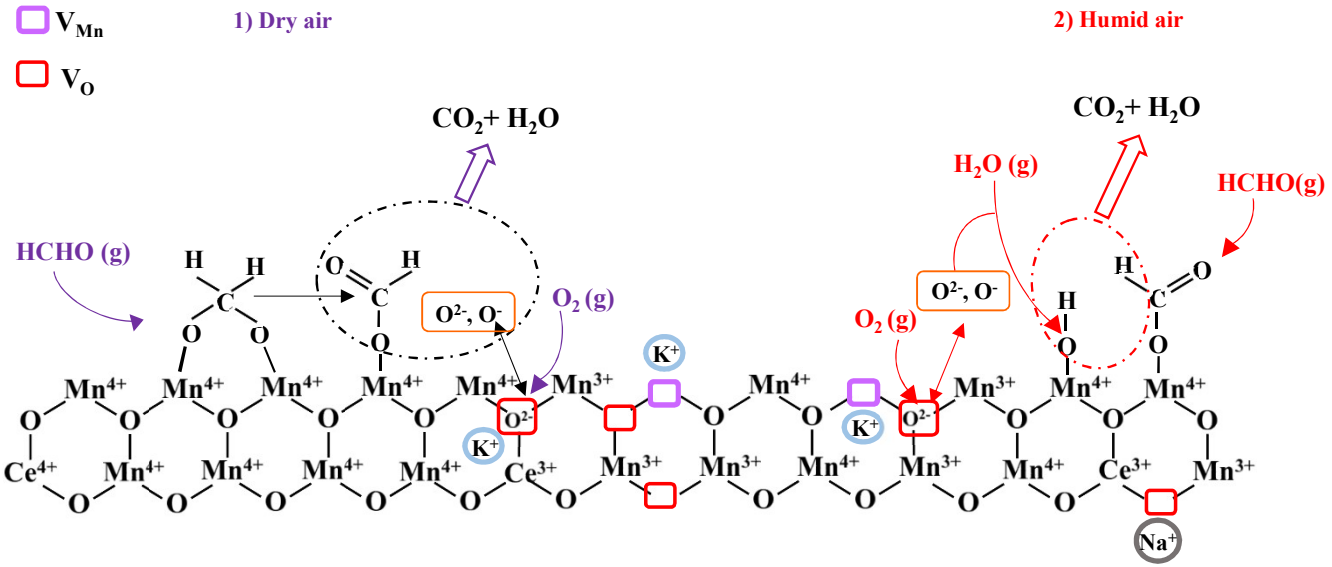
V_Mn
V_O
1) Dry air
2) Humid air
CO2+ H2O
CO2+ H2O
H2O (g)
HCHO (g)
HCHO(g)
O2 (g)
O2 (g)
O2-, O-
O2-, O-
K+
K+
K+
Na+
Mn4+
Mn3+
Ce3+
O2-

Table 1: ICP-OES analysis of the as-synthesized samples

Catalyst	Weight %				Atomic ratio		
	K	Na	Ce	Mn	K/Mn	Na/Mn	Ce/Mn
Mn-B	7.12	1.87	-	44.1	0.39	0.059	-
$Ce_{0.01}Mn$	6.64	2.08	1.11	46.4	0.34	0.063	0.0094
$Ce_{0.1}Mn$	6.27	1.90	9.47	38.3	0.39	0.069	0.097

Table 2: Weight loss as a function of temperature for the as-synthesized and calcined samples

Catalyst	Total loss (%)	25-220°C (100-220°C) (%)	220°C-T_t* (%)	Weight gain (%)
Mn-B	15.8	10.7 (6.8)	5.1 (-)	-
$Ce_{0.01}Mn$	14.4	11.1 (7.6)	3.4 (520)	0.14
$Ce_{0.01}Mn$-300	11.0	9.0 (5.3)	2.3 (525)	0.30
$Ce_{0.01}Mn$-400	7.2	5.4 (4.0)	1.9 (554)	0.12
$Ce_{0.1}Mn$	14.3	10.5 (7.3)	4.4 (680)	0.60
$Ce_{0.1}Mn$-200	10.6	5.2 (3.9)	5.6 (676)	0.23
$Ce_{0.1}Mn$-300	7.8	4.3 (2.8)	3.9 (670)	0.49
$Ce_{0.1}Mn$-400	7.4	5 (3.1)	2.9 (674)	0.52

T_t*: Temperature of phase transformation

Table 3: Crystallite size (D), Textural/redox and XPS characterizations of the fresh and samples calcined at 400°C

Catalyst	D (nm)	$S_{pecific\ area}$ (m^2/g)	n (H_2) ($mmol/g_{cat}$)	XPS			
				K/Mn	Na/Mn	Ce/Mn	Mn^{3+}/Mn^{4+}
Mn-B	4.8	44	7.55	0.28	0.13	-	0.24
Mn-B-400	3.2	148	9.13	0.24	0.089	-	0.30
$Ce_{0.01}Mn$	3.3	127	7.03	0.24	0.12	0.016	0.18
$Ce_{0.01}Mn$-400	3.2	132	9.28	0.18	0.049	0.015	0.33
$Ce_{0.1}Mn$	n.d.	243	4.93	0.21	0.12	0.13	0.17
$Ce_{0.1}Mn$-400	n.d.	196	7.65	0.19	0.080	0.11	0.37

Table 4: ToF-SIMS results

Catalyst	Ce^+/Mn^+	CeO^+/Ce^+	$CeOMn^+/(Ce^+ + Mn^+)$ $\times 10^3$
$Ce_{0.01}Mn$	0.0020	5.99	0.87
$Ce_{0.01}Mn$-400	0.023	0.37	1.43
$Ce_{0.1}Mn$	0.015	13.19	7.09
$Ce_{0.1}Mn$-200	0.057	3.07	10.32
$Ce_{0.1}Mn$-300	0.029	4.75	9.26
$Ce_{0.1}Mn$-400	0.042	3.36	10.89

Table 5: Catalytic results

Catalyst	T_{10} (°C)	T_{50} (°C)	T_{90} (°C)
Mn-B-400	69	101	124
$Ce_{0.01}Mn$-300	-	56	80
$Ce_{0.01}Mn$-400	-	50	73
$Ce_{0.1}Mn$-200	37	78	107
$Ce_{0.1}Mn$-300	25	68	96
$Ce_{0.1}Mn$-400	-	56	90